Continent and Life Evolution

OPEN ACCESS
Article

Obliquity-modulated poleward rain-belt shifts recorded in the Pliocene-Pleistocene sequence, northern Chinese Loess Plateau

Minghao Ma, Rui Zhang*, Lu Sun, Leping Yue and Hujun Gong*

*** E-mails:** ruizhang@zjnu.edu.cn; gonghujun@nwu.edu.cn

Received 25 August 2025; Revised 24 December 2025; Accepted 12 January 2026; Published 24 April 2026

https://doi.org/10.55092/cle20260004

Graphical Abstract

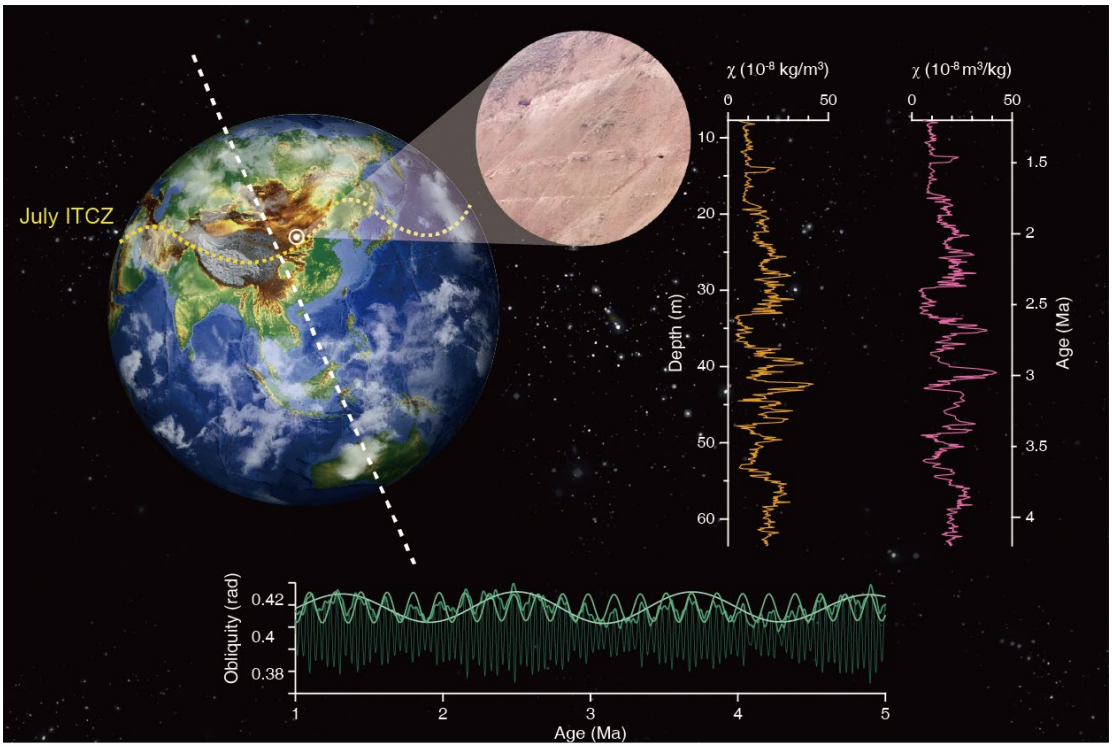

Highlights:

- Robust 405 kyr, 173 kyr, and ~1.2 Myr bands pace hydroclimate on the northern CLP.
- Age model tuned to 173 kyr obliquity modulation, validated by 405 kyr eccentricity.
- Obliquity amplitude envelopes align with regional χ stacks and deep-ocean $\delta^{18}O/\delta^{13}C$.

Obliquity-modulated poleward rain-belt shifts recorded in the Pliocene-Pleistocene sequence, northern Chinese Loess Plateau

Minghao Ma[1], Rui Zhang[2,*], Lu Sun[3], Leping Yue[1] and Hujun Gong[1,*]

[1] State Key Laboratory of Continental Evolution and Early Life, Department of Geology, Northwest University, Xi'an 710069, China

[2] College of Geography and Environmental Sciences, Zhejiang Normal University, Jinhua 321004, China

[3] School of Earth Sciences, East China University of Technology, Nanchang 330013, China

E-mail: ruizhang@zjnu.edu.cn; gonghujun@nwu.edu.cn.

Abstract: Earth's axial tilt modulates meridional insolation gradients and, in turn, the latitude of the tropical rainbelt/Intertropical Convergence Zone (ITCZ). We test this mechanism at the northern limit of the Asian summer monsoon using a 63.5-m red clay–loess succession on the northern Chinese Loess Plateau (CLP). New magnetic susceptibility (χ) and grain-size (< 5 μm) series, anchored by magnetostratigraphy and refined by astronomical tuning, reveal statistically significant 405 kyr eccentricity, ~173 kyr obliquity modulation, and ~1.2 Myr bands. We iteratively tuned the χ series to the astronomical solution using the ~173 kyr obliquity-modulation filter, and independently validated the chronology against the 405 kyr eccentricity band; evolutive spectral analysis further verifies the cyclic pacing and phase relationships. Band-pass reconstructions show that χ maxima broadly coincide with obliquity amplitude highs, consistent with strengthened summer monsoon and northward rainbelt displacement. Coherence with χ from nearby CLP sections (Wujiamao, Lingtai) and with benthic δ18O–δ13C further supports regional to global controls. We interpret the CLP record as an obliquity-gated archive of ITCZ poleward pulses during the Pliocene-Pleistocene, modulated by 173 kyr (Earth-Saturn) and ~1.2 Myr (Earth-Mars) beats, superposed on the long-eccentricity metronome. The tuned framework provides a physically grounded chronology for future multi-proxy work and a benchmark for testing monsoon-ITCZ dynamics in warm-climate simulations.

Keywords: Chinese Loess Plateau; Wuqi; magnetic susceptibility; astronomical tuning; obliquity; 173 kyr; 405 kyr; ITCZ; Asian monsoon

1. Introduction

Earth's obliquity primarily controls the latitudinal pattern of annual-mean top-of-atmosphere insolation—a steeper tilt increases annual insolation at high latitudes and decreases the equator-to-pole gradient, whereas a reduced tilt does the opposite effect (Laskar *et al.* 2011). Variations in tilt arise from gravitational coupling within the Sun-Earth-Moon-planet system and are expressed as a family of cycles centered near ~41 kyr, further modulated by longer beats tied to planetary terms—most prominently the Earth-Saturn ~173 kyr and the Earth-Mars ~1.2 Myr bands that emerge from astronomical solutions (Hinnov 2013; Laskar 2020) These slow modulations alter the background state on which synoptic and seasonal processes operate and, in principle, can drive coherent, low-frequency structure in continental hydroclimate archives when the transfer function integrates climate over multiyear to millennial scales (Qin *et al.* 2022; Zhang *et al.* 2022).

The meridional insolation gradient is the immediate conduit by which obliquity acts on the atmosphere (Cao *et al.* 2025; Li *et al.* 2025). When the gradient increases, the Hadley cell widens, the ITCZ shifts in latitude, and the East Asian summer monsoon (EASM) rain-belt penetrates farther poleward; when the gradient relaxes, the opposite occurs. Moisture delivered to the EASM is ultimately sourced in the Indo-Pacific Warm Pool (IPWP), yet the latitude of ascent and the duration of monsoon seasons reflect both the ITCZ position and the thermal forcing over the Tibetan Plateau and its forelands (Wei *et al.* 2025). Soil formation and landscape evolution are driven by processes unfolding over long timescales (105–106 years), endowing these terrestrial systems a unique ability to faithfully record long-period obliquity modulations and eccentricity variations. This match between the integrative memory of terrestrial systems and the timescales of orbital forcing is especially striking near rain-belt margins: small north-south shifts of the rain belt here trigger significant changes in effective moisture, and these shifts in turn leave distinct orbital signatures in the environment (Li *et al.* 2022) (Figure 1). Recent syntheses and reconstructions support this linkage between obliquity, insolation gradients, and monsoon-ITCZ dynamics (Ma *et al.* 2025; Zhang *et al.* 2025) From the Pliocene into the Pleistocene, Earth's boundary conditions approached modern states as meridional and zonal sea-surface-temperature (SST) gradients sharpened and tropical overturning reorganized (Brierley and Fedorov 2010; Fedorov *et al.* 2015). Northern Hemisphere ice sheets expanded and seasonality strengthened, amplifying monsoon variability and sharpening the orbital imprint (Wang *et al.* 2019; Westerhold *et al.* 2020). Over the same interval, eccentricity envelopes modulated precession

forcing, while obliquity pacing intermittently emerged in continental hydroclimate. The Chinese Loess Plateau (CLP) red clay–loess succession is particularly sensitive to these low-frequency bands owing to its combined eolian-pedogenic nature (Laskar *et al.* 2004; Nie *et al.* 2008; Sun *et al.* 2010).

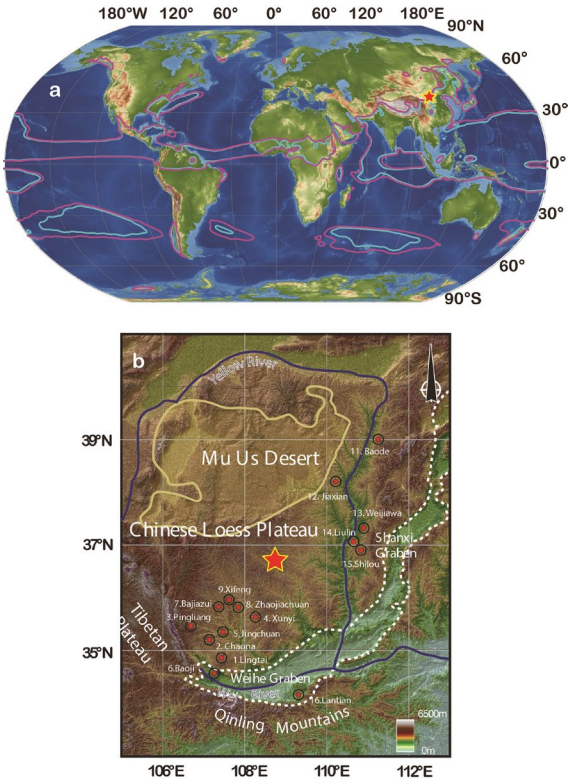

Figure 1. Location, modern summer precipitation pattern and stratigraphic setting of the Wuqi section. **(a)** Present-day global topographic map. The red and blue lines represent simulation summer precipitation levels of 350 mm and 400 mm before the industrial evolution (Li *et al.* 2022), respectively, during June, July, and August. The yellow star indicates the studied Wuqi section; **(b)** Site map and stratigraphic overview for the Wuqi section on the northern CLP, showing topography, regional setting relative to the Mu Us Desert.

The intensification of 405 kyr eccentricity signal expression has been detected in both paleoclimate proxies in the CLP and benthic oxygen isotopes records, making it a key tool for establishing high-resolution sequences (Nie 2018; Su and Nie 2024; Wang *et al.* 2025). Previous studies link this climate event to drivers including Tibetan Plateau uplift, Arctic ice sheet onset, and oceanic salinity/SST differences (Nie *et al.* 2008; Sun *et al.* 2010; Nie 2018). Another geologically stable periodicity—the 173 kyr cycle—has been validated as a reliable stratigraphic calibration metronome through case studies, influencing local precipitation and carbon cycles (Boulila *et al.* 2018; Huang *et al.* 2021; Li *et al.* 2024). However, 173 kyr obliquity amplitude cycles have rarely been reported in the CLP records. 173 kyr cycles in the CLP were first detected at the Wujiamao Section with sedimentation at this section terminating prior to 3 Ma (Zhang *et al.* 2022), while a revised age model of Shilou Section remains controversial (Anwar *et al.* 2015; Xu and Chen 2024).

Although numerous CLP studies have emphasized the dynamically stable 405 kyr long-eccentricity signal, tuning directly to that target can blur causal interpretation when dust supply itself is partly eccentricity-paced. A complementary strategy is to use the physically motivated ~173 kyr obliquity modulation as the primary alignment and reserve the 405 kyr term for independent validation, thereby decoupling tuning from verification (Laskar *et al.* 2004; Nie *et al.* 2008; Sun *et al.* 2010; Zhang *et al.* 2022). This approach allows tests of whether tilt-linked envelopes organize hydroclimate variability at the poleward monsoon margin and whether the phases recovered from continental archives are consistent with expectations for ITCZ latitude and seasonal duration set by the meridional insolation gradient (Li *et al.* 2022, 2025; Cao *et al.* 2025; Ma *et al.* 2025; Wei *et al.* 2025).

At the northern CLP margin, the Wuqi section sits along the Baiyu Mountains front, near the climatological limit of the EASM rainbelt. Here magnetic susceptibility (χ) and fine fraction (< 5 μm) respond to modest shifts in moisture and weathering and thus provide a strategic test of whether the ~173 kyr and ~1.2 Myr obliquity-related bands organize hydroclimate variability alongside the dynamically stable ~405 kyr eccentricity pacing (Anwar *et al.* 2015; Qin *et al.* 2022; Zhang *et al.* 2022; Wei *et al.* 2025). This study documents the expression of ~173 kyr, 405 kyr, and ~1.2 Myr bands in χ and grain size at Wuqi; establishes a chronology by tuning to ~173 kyr with the geomagnetic polarity time scale (GPTS) as a hard constraint; and evaluates physical links among tilt amplitude, ITCZ latitude, and monsoon reach through comparisons with regional χ stacks (e.g. Wujiamao, Lingtai) and the marine benthic stack. Our aim is to provide a chronology and mechanism that are simultaneously statistically robust and dynamically interpretable to the Asian monsoon system.

2. Geological setting and stratigraphy

The studied section (36°48′33.7″N, 108°15′34.4″E) lies on the southern flank of the Baiyu Mountains in the northern CLP, where an E-W ridge between ~1200 and 1800 m a.s.l. separates the Mu Us Desert from the loess domain (Figure 1). This physiographic boundary coincides with the northern reach of the Asian summer monsoon rainbelt, making the site acutely sensitive to obliquity-driven changes in the meridional insolation gradient and associated ITCZ displacements (Qin *et al.* 2022; Zheng Y *et al.* 2022). The exposed composite is ~63.5 m thick and rests unconformably on Triassic sandstones and shales of the Ordos Basin, providing continuous outcrop and fresh surfaces suitable for systematic sampling and paleomagnetic work investigations (Sun *et al.* 2010). Comparable facies patterns and regional correlations have been reported from other CLP localities (Ding *et al.* 1998; Nie *et al.* 2008; Sun *et al.* 2010; Sun *et al.* 2010; Liu *et al.* 2015;

Maher 2016; Gradstein *et al.* 2020; Qin *et al.* 2022; Zhang *et al.* 2022; Zheng Y *et al.* 2022; Cao *et al.* 2025; Li *et al.* 2025; Wei *et al.* 2025) (Figure 1b).

Lithostratigraphy documents a progressive transition from pedogenically reworked red clay to dustier, more weakly altered primary loess. From base to top we distinguish six units (Figure 2a): (i) ~10.5 m of relatively pure red clay with scattered calcareous nodules and variegated muddy lenses; (ii) 15.8 m of red clay showing increasing calcareous cementation and faint bedding with gray-white, brown-yellow, and gray-green silty-muddy clasts as reworked aggregates; (iii) 3.6 m of red clay enriched in gray-green to gray-white muddy/silty granules and calcareous specks with abundant vertebrate fossil fragments; (iv) 10.8 m of darker reddish-brown fine loess with thin calcareous interlayers; (v) 15.3 m chiefly of brown-yellow to brown-red loess with minor gray-white to gray-green muddy-silty interbeds; and (vi) a 7.7 m soft, brown-yellow Malan Loess cap across a gently erosive contact. Fossiliferous horizons and carbonate bands provide internal constraints on proxy interpretations tied to weathering intensity and hydrologic balance. Observations from adjacent basins further corroborate this stratigraphic framework (Qin *et al.* 2022; Zhang *et al.* 2022; Cao *et al.* 2025).

The polarity framework comprises ten magnetozones (Figure 2) (Gradstein *et al.* 2020). The measured section (the overlying Malan Loess Brunhes were removed during trimming) begins within the Matsuyama Chron at the reversed subchron C1r.3r, which forms the uppermost magnetozone (R1). Down-section, the Olduvai Normal Chron follows (N1 = C2n), succeeded by a reversed interval (R2 = C2r). The Gauss interval includes three normal zones (N2–N4) separated by the Kaena and Mammoth (R3–R4), and it overlies the lower Gilbert reversed zone (R5 = C2Ar) and basal Cochiti normal (N5 = C3n.1n). Reversal boundaries are sharp and reproducible within two sampling steps, enabling confident correlation to the Geologic Time Scale (GPTS) and placing the base at ~4.28 Ma. Regionally, the northern CLP forms the downwind foreland of the Tibetan Plateau and the Ordos margin; orographic effects amplify modest shifts in jets and monsoon fronts, explaining both the high sensitivity of χ to hydroclimate and the coherence with Wujiamao and Lingtai χ stacks (Sun *et al.* 2010; Anwar *et al.* 2015). Comparable facies patterns and regional correlations have been reported from other CLP localities, and observations from adjacent basins further corroborate this stratigraphic framework (Ding *et al.* 1998; Qin *et al.* 2022; Zhang *et al.* 2022; Cao *et al.* 2025).

3. Methods

3.1. Sampling and laboratory analyses

We collected 590 powder samples along the section at 10cm spacing (20 cm within the upper 7.7 m Malan Loess) for paired magnetic susceptibility and grain size measurements. Surfaces were trimmed to remove weathered rinds and each specimen was homogenized to minimize microscale heterogeneity. Low frequency magnetic susceptibility (976 Hz) was measured using an AGICO MFK2FA Kappabridge in the Paleomagnetism Laboratory, State Key Laboratory of Continental Dynamics, Northwest University; a running standard indicates < 1% drift, and 10% blind replicates demonstrate ± 2% reproducibility. Grain size distributions were measured on the same suite of samples with a Malvern Mastersizer 2000, plus ~200 additional specimens at intervals of rapid lithologic change. Pretreatment followed a standard CLP protocol: removal of organics with 10% H_2O_2, dissolution of carbonates with 10% HCl, repeated rinsing and decanting after 12-hour settling, deflocculation with 0.05 mol/L sodium hexametaphosphate ($(NaPO_3)_6$), and ~10 min ultrasonication immediately prior to measurement.

3.2. Original data processing and time-series analysis

The χ and < 5 μm series were processed in Acycle v2.8 to remove outliers, resample to equal spacing by linear interpolation, and detrend with LOWESS (span = 0.5) following best practice in cyclostratigraphy (Thomson 1982; Li *et al.* 2019). Under the magnetostratigraphic age model (Sun *et al.* 2010), we computed multi-taper spectra (time-band-width product 2–3; 3–5 tapers) and evolutive harmonic analysis (EHA) with an 1800 kyr sliding window and 50% overlap to detect Milankovitch bands and their persistence. Significance was assessed using both AR(1) and smoothed window averaging (SWA) methods to evaluate reliability: confidence intervals for AR(1) were calculated, while false discovery rate (FDR) control was applied to compute confidence intervals for SWA. Guided by persistent peaks, we applied Gaussian bandpass filters to proxies and to the astronomical target (La2010/2011) to isolate the ~1.2 Myr obliquity modulation, 405 kyr long eccentricity, and ~173 kyr obliquity modulation bands (Laskar *et al.* 2011; Laskar 2020). Evolutionary FFT (eFFT) was used to analyze time-frequency characteristics, complementing spectral techniques by resolving time-varying periodicities via sliding window transformations. Our methodology follows established practices in cyclostratigraphic detection and significance assessment (Anwar *et al.* 2015; Zhang *et al.* 2021; Wei *et al.* 2025; Zhang *et al.* 2025).

3.3. Astronomical tuning

To refine the chronology, we first aligned the data to the ~1200 kyr obliquity amplitude cycle, following which we implemented two tuning schemes: the conventional 405 kyr eccentricity cycle tuning and the ~173 kyr obliquity amplitude cycle tuning. Both schemes were constrained by the La2010/2011 solution under GPTS constraints. For each scheme, χ and the target astronomical signals were bandpass filtered around their respective target periods using a Gaussian filter (0.002–0.003 cycles/kyr for 405 kyr and 0.005–0.0065

cycles/kyr for 173 kyr). Tuning points were iteratively matched to minimize phase misfit while preserving the spacing among tie-points. The tuned solution was accepted only if coherence to the targets improved across multiple windows. Spectral and wavelet analyses were implemented following widely recommended procedures (Ma *et al.* 2025; Zhang *et al.* 2025; Zhang *et al.* 2025).

4. Results

4.1. Paleoclimate proxies

Low-frequency magnetic susceptibility (χ) exhibits millimeter- to centimeter-scale variability superposed on meter-scale trends (Figure 2). In the eolian sediment interval, χ generally coincides with subtle reddening and weak pedogenic structures. The clay-size fraction (< 5 μm) varies consistently with χ at multi-decimeter to multi-meter scales, periods of enhanced pedogenesis (indicated by higher χ) correspond to increased proportions of the < 5 μm fraction, reflecting weakened primary eolian input. Cross-plots show a positive relationship between χ and the < 5 μm fraction, except in the topmost ~10 meters, implying that the sensitivity of χ to fine-fraction variations increases, and that both proxies covary as the system shifts from dustier loess deposition to red clay pedogenesis. Carbonate-rich horizons correspond to local χ minima and positive spikes in median grain size, consistent with reduced weathering intensity.

Figure 2. Integrated stratigraphy, magnetic susceptibility

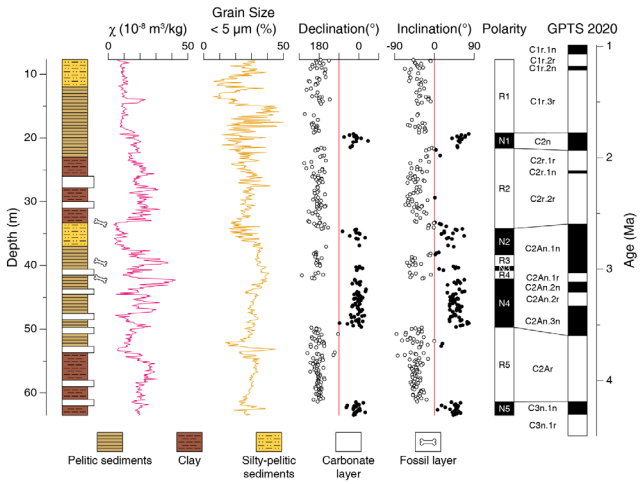

(χ), < 5 μm fraction, carbonate layers, and magnetozones (Brunhes-Matsuyama-Gauss-Gilbert with subchrons) correlated to GPTS 2020 (Gradstein *et al.* 2020).

4.2. Astronomical periodicities

Under the magnetostratigraphic age model, multi-taper spectra reveal significant power at ~405 kyr, ~173 kyr, and ~1.2 Myr with weak, intermittent precession signals (Figure 3). Evolutive analyses indicate that the 405 kyr cycle persists across the section, whereas the ~173 kyr cycle intensifies upward in parallel with higher χ variance. Guided by these periodicities we respectively aligned the ~173 kyr and ~405 kyr bands of χ to the La2010/2011 astronomical solution under polarity constraints using a Gaussian bandpass (±12–15%) (Figure 4) (Laskar *et al.* 2011). Our 173 kyr and 405 kyr tuning schemes yield comparable trends and sedimentation rates (Figure 4), with both resolving a prominent ~1.2 Myr cycle that aligns robustly with the corresponding periodicity in the La2010/2011 astronomical model. Across multiple sliding windows, both models also exhibit near-zero phase lag relative to their respective target cycles, validating their astronomical tuning credibility. Notwithstanding these shared strengths, the two schemes differ distinctly in their spectral characteristics (Figure 5). The 405 kyr-tuned χ record is restricted to the ~1.2 Myr and 405 kyr cycles, whereas the 173 kyr-tuned counterpart also captures a clear in-phase 405 kyr cycle—consistent with independent eccentricity forcing. Coupled with the consistency of primary periodicities in the pre-tuning (magnetostratigraphic) spectrum, the 173 kyr tuning model is thus selected for subsequent analyses. Regional χ stacks and benthic compilations exhibit compatible pacing and phases with our record (Sun *et al.* 2010; Boulila *et al.* 2018; Westerhold *et al.* 2020; Zhang *et al.* 2022) (Figure 6).

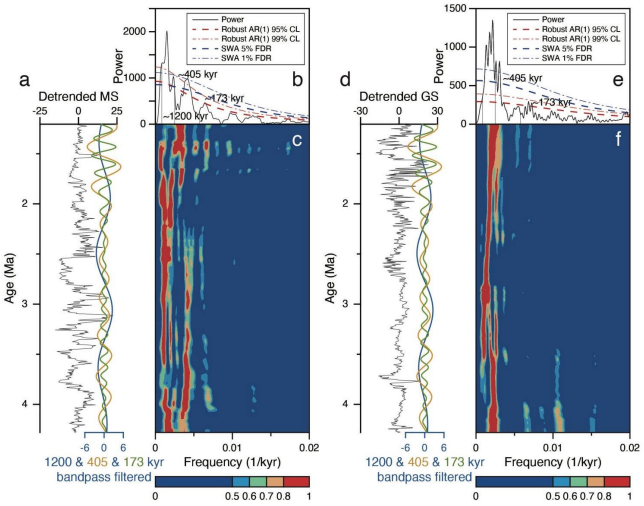

Figure 3. Spectral analyses under the initial (magnetostratigraphic) age model: MTM spectra and EHA/wavelet for χ highlighting significant bands near ~405 kyr, ~173 kyr, and ~1.2 Myr; Gaussian band-pass reconstructions shown for target comparison.

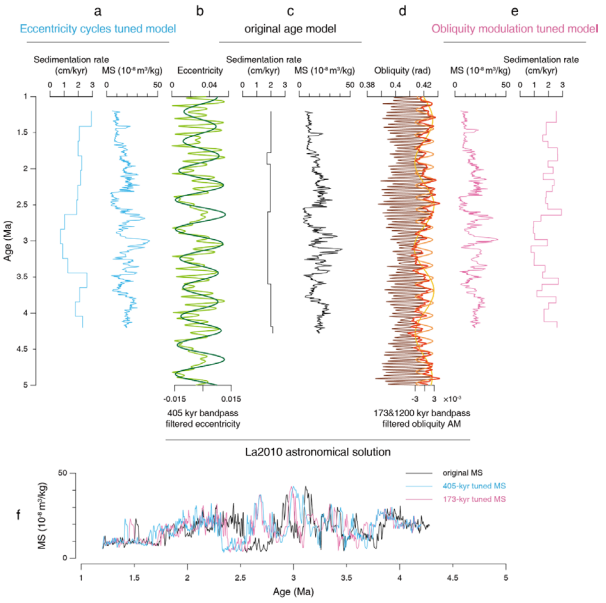

Figure 4. Tuning to the ~405-kyr eccentricity (blue) and ~173-kyr obliquity-modulation (pink) targets: band-pass alignment, tie-points, phase misfit diagnostics, and resulting age-dept function.

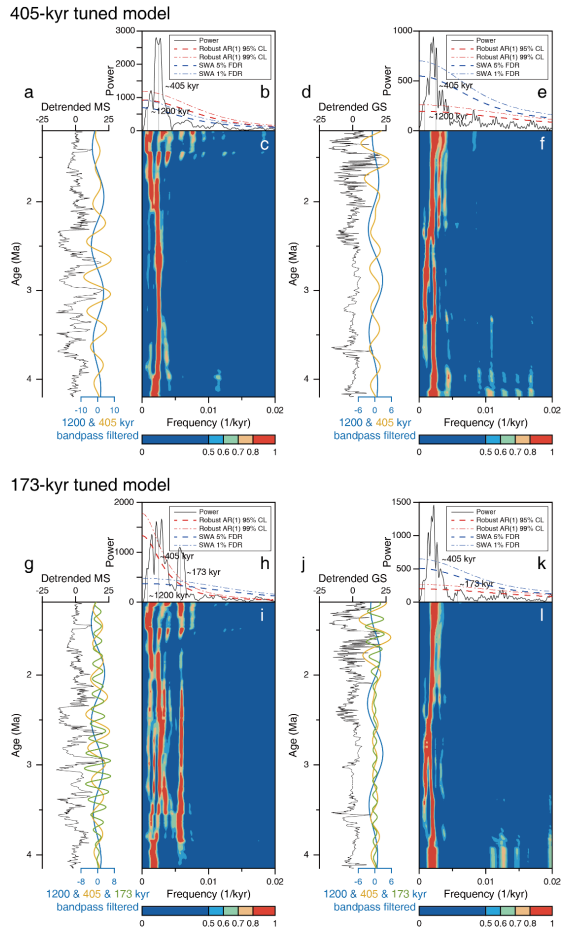

Figure 5. Spectral analyses of χ and the < 5 μm grain-size fraction derived from the post-tuning models for Wuqi Section. A stable coherence to 405-kyr eccentricity was also detected in the 173-kyr obliquity-targeted tuning model.

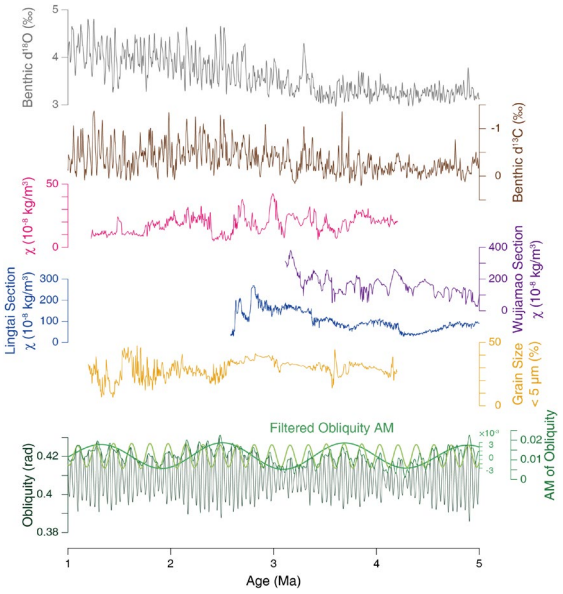

Figure 6. Regional and global comparisons: Wujiamao (Zhang *et al.* 2022) and Lingtai χ stacks (Zhang *et al.* 2022), envelope amplitude, and Marine δ18O-δ13C stacks (Westerhold *et al.* 2020) aligned to the tuned chronology, emphasizing shared pacing and phase relations.

The 173 kyr-tuned age-depth relation implies gradually increasing sedimentation rates from red clay into loess, consistent with a shift toward dust-rich conditions, with an average rate of 1.86 cm/kyr, which is considered to be a similar value in CLP red clay sections. Phase analysis shows both χ and < 5 μm fraction are in phase with the ~173 kyr target and with obliquity amplitude highs. At 405 kyr, χ and the eccentricity target are phase locked within uncertainty, consolidating the dual control of precession-modulated hydro-pedogenesis and eccentricity-paced dust supply. Regional comparison to Wujiamao and Lingtai χ stacks (Ding *et al.* 1998; Sun *et al.* 2010; Zhang *et al.* 2022) demonstrates near-zero-lag correlation at 405 kyr and shared low frequency envelopes, while alignment with the marine stack suggests concurrent changes in ice volume and carbon cycling during intervals of stronger monsoon reach (Westerhold *et al.* 2020).

5. Discussion

5.1. Age model of Wuqi Section

The astronomically tuned age model is generally consistent with magnetostratigraphic results, though minor discrepancies persist, especially in the middle-lower interval corresponding to N2–N4 in (Figure 2). This interval is distinguished by fine-grained sediments, low sedimentation rates, and frequent carbonate layers. Remanent magnetism in sediments is only preserved after deposition and consolidation, and can be altered by post-depositional leaching. Such processes introduce a measurable time lag between the actual sedimentation time and the period when remanent magnetization is finally recorded.

Field observations confirm the overall continuity of the sedimentary sequence at the Wuqi section, with continuous variations in χ and grain size profiles providing further support. Sedimentation across the CLP is strongly influenced by the East Asian Winter Monsoon, which intensified at ~4.0 Ma with the onset of Arctic glaciation and maintained a close linkage to glacial dynamics thereafter (De Schepper *et al.* 2014; Westerhold *et al.* 2020). The Jingbian section at the northern CLP has recorded short-lived sedimentary hiatuses triggered by glacial activities (Stevens *et al.* 2018). Besides, a rapid uplift of the Baiyu Mountains from 1.5 to 0.8 Ma was interpreted from the increase in median grain size from the nearby Hegou profile (Xu *et al.* 2025), as reflected in our data since ~1.5 Ma, causing potential hiatuses as well. The lower Wuqi section may have experience similar but far milder hiatus events, attributed to the relatively limited scale of glaciation during the late Pliocene (De Schepper *et al.* 2014). These hiatuses are shorter in duration than the orbital cycles used for astronomical tuning, so the overall age framework of the tuned model remains reliable. However, such discontinuities can disrupt precise positional alignment during tuning, leading to minor deviations in fine-scale age estimates. Together with the post-depositional modification of remanent magnetism, these factors collectively explain the minor discrepancies between the astronomically tuned age model and magnetostratigraphic results.

5.2. Astronomical forcing and climate evolution characteristics

The Wuqi Section provides a unique insight into the astronomical forcing on the CLP from the late Pliocene to the early Holocene. The expansion of Arctic ice sheets and the Mu Us Desert at the boundary between Pliocene and Pleistocene at ~2.6 Ma (Stevens *et al.* 2018), caused a sudden aridification and coarser sediments as reflected in the χ and grain size, respectively. Although the astronomical forcing drivers remain stable across this transition as shown in (Nie *et al.* 2008) and this study, the proxies in the Wuqi section reveal an eccentricity-and-obliquity-paced climate evolution, while the migration of the Mu Us Desert did not distort the record of rain-belt shifts in the northern CLP. Eccentricity is rather weak in influencing local hydroclimate but exerts its effect by modulating precession, thereby influencing the insolation and evaporation in the low-latitude areas. Obliquity-paced rain-belt dynamics at the northern CLP margin emerge from a physically constrained chain linking tilt-driven meridional insolation gradients to the latitude and persistence of tropical ascent. In soils that integrate hydroclimate over multi-year to decadal windows, this slow forcing projects efficiently into χ through pedogenic enhancement (Liu *et al.* 2005, 2015; Sun *et al.* 2010). As synthesized in (Figure 6), regional χ stacks and marine benthic comparators highlight shared pacing and phase relations under the tuned chronology. Our tuned chronology intentionally targets the ~173 kyr obliquity-modulation band, using the long-eccentricity (405 kyr) signal only as an independent check. This design minimizes circularity where dust supply may itself be eccentricity paced, and it leverages the direct dynamical pathway from tilt amplitude to the annual-mean meridional insolation gradient and the ITCZ latitude (Laskar *et al.* 2004; Hinnov 2013; Zhang *et al.* 2022).

Cross-spectral analyses substantiate this strategy: tuned χ exhibits near-zero-lag coherence with the 173 kyr target and, crucially, strong and stable coherence with the independent 405 kyr target across long intervals—evidence that eccentricity pacing emerges from the data rather than being imposed by tuning. Regional χ stacks (Wujiamao, Lingtai) and benthic compilations show compatible pacing and phases (Figure 6). reinforcing that the Wuqi signal is both local and regionally coherent (Lisiecki and Raymo 2005; Sun *et al.* 2010; Westerhold *et al.* 2020). The clarified ~1.2 Myr envelope in χ aligns with expectations from planetary-term modulation of obliquity; amplitude nodes and antinodes correspond to predicted minima and maxima in tilt amplitude, consistent with an integrative pedogenic transfer function operating at rain-belt margins (Hinnov 2013; Qin *et al.* 2022).

Orography magnifies the low-frequency forcing. The Tibetan Plateau strengthens land-sea thermal contrasts and anchors stationary waves, such that modest shifts in jets and monsoon fronts can therefore yield large local hydroclimatic responses at the northern CLP, expanding the dynamic range of χ relative to interior sites (An *et al.* 2001; Wu *et al.* 2022). The Pliocene-Pleistocene background against which these bands operate featured sharpening meridional/zonal SST gradients and reorganized tropical overturning, with implications for the ITCZ and the monsoon reach. Model-data syntheses indicate that gradient-driven circulation changes modulate the latitude of tropical convection, providing a complementary route by which tilt-linked insolation gradients are expressed in rainfall (Brierley and Fedorov 2010; Fedorov *et al.* 2015; Burls *et al.* 2017). Larger axial tilt expands the tropics, exposing more coastal areas to intense solar radiation. This enhances sea evaporation, which in turn carries extra atmospheric moisture inland, reinforcing the hydroclimatic responses at the northern CLP under more favorable topographic conditions induced by the uplift of the Tibetan Plateau.

Coherence between χ peaks and lighter benthic δ18O, together with positive δ13C excursions in global stacks, points to intervals of reduced global ice volume and invigorated carbon cycling coincident with poleward rain-belt excursions—consistent with enhanced silicate weathering and terrestrial productivity under stronger monsoon conditions (Lisiecki and Raymo 2005; Westerhold *et al.* 2020). Moisture supply ultimately originates from the Indo-Pacific Warm Pool (IPWP). As the temperature of the IPWP rises, atmospheric convective activity in the warm pool region intensifies, releasing

substantial latent heat and stimulating upward atmospheric motion, shifting the intensity and position of the Walker circulation and the Hadley circulation. Warming of the IPWP leads to strengthened upward motion in the western Pacific within the Walker circulation, and to intensified meridional circulation in the Hadley circulation. The $\delta^{18}O$ record from ODP Site 806 provides evidence that the modern Walker circulation was established at ~3.7 Ma (Wycech *et al.* 2020). Observations indicate that modest shifts in the mean latitude of ascent and Walker/Hadley circulations strongly affect monsoon rainfall delivered to East Asia. Such teleconnections render the Wuqi site especially responsive to low-frequency changes in the large-scale circulation (Qu *et al.* 2005; Oppo *et al.* 2009). Eccentricity remains dynamically stable and prominent in dust-supply proxies, yet our 173 kyr-first approach demonstrates that the 405 kyr pacing is independently recovered and phase-stable. This orthogonality—tilt-targeted tuning plus eccentricity validation—aligns with best-practice guidance for spectral detection, significance testing, and the avoidance of over-interpretation in mixed pedogenic-eolian archives (Miller *et al.* 2001; Hinnov 2013; Weedon 2022).

Methodologically, our results are robust to alternative detrending schemes, bandwidth selections, and jackknife tests, and they are supported by multi-method significance controls (robust AR(1) and SWA backgrounds with false-discovery-rate adjustment). These safeguards reduce the chance of spuriously identifying orbital bands in noisy terrestrial series (Miller *et al.* 2001). The Wuqi record thus provides a benchmark obliquity-gated archive for testing warm-climate simulations. Models capable of reproducing persistent 405 kyr pacing and bundled, tilt-modulated pulses at the ~173 kyr scale (nested within a ~1.2 Myr envelope) likely capture the key orographic and land-sea contrast processes that govern monsoon reach (Fedorov *et al.* 2015; Dowsett *et al.* 2016; Burls *et al.* 2017). Finally, the spatial gradient across the CLP suggests that margin sites emphasize hydroclimate signals, whereas interior sites reflect a mix of sediment transport and pedogenic modification. Coordinated transects, coupled with isotopic and elemental proxies, will help separate latitude-driven from source-driven variability and clarify how slowly varying orbital geometry organizes continental hydroclimate (Tian *et al.* 2008; Sun *et al.* 2010; Liu *et al.* 2015).

6. Conclusion

The Wuqi section records statistically robust ~1.2 Myr, 405 kyr, and ~173 kyr bands in χ and grain size; precession is weak and intermittent, consistent with pedogenic integration at the rainbelt margin. Tuning χ to the ~173 kyr obliquity modulation band under magnetostratigraphic constraints yields a stable chronology that is validated, not imposed—by strong, independent coherence to 405 kyr. Maxima in χ and < 5 μm fraction align with obliquity amplitude highs, implying tilt-gated poleward excursions of the Asian summer rainbelt at the CLP's northern edge. Regional and global coherences indicate coupled hydroclimate-carbon system dynamics on obliquity-related timescales. The tilt-centric tuning and validation framework offers a transferable template for cyclostratigraphy analysis in mixed pedogenic-eolian archives and a quantitative target for warm climate model evaluation.

Data availability statement

The data or datasets that support the findings of this study are available from the corresponding author upon reasonable request.

Declaration of generative AI and AI-assisted technologies

During the preparation of this manuscript, the authors used generative AI tools only to improve language and readability. The authors take full responsibility for the content of the manuscript.

Acknowledgments

This work was funded by the National Nature Science Foundation of China with grant number 41772027, and the State Key Laboratory of Loess Science (grant SKLLQG2104).

Authors' contribution

Conceptualization, R.Z. and M.M.; fieldwork, L.Y. and L.S.; experiments, M.M. data processing, M.M.; data curation, R.Z. and M.M.; writing—original draft preparation, R.Z. and M.M.; writing—review and editing, R.Z. and H.G.; project administration, R.Z.; funding acquisition, R.Z. All authors have read and agreed to the published version of the manuscript.

Conflicts of interest

No potential conflict of interest was reported by the authors.

References

An Z, Kutzbach JE, Prell WI, Porter SC. Evolution of Asian monsoons and phased uplift of the Himalaya-Tibetan plateau. *Nature* 2001, 411(6833):62–66. DOI: 10.1038/35079500

Anwar T, Kravchinsky VA, Zhang R. Magneto- and cyclostratigraphy in the red clay sequence. *J. Geophys. Res.: Solid Earth* 2015, 120(10):6758–6770. DOI: 10.1002/2015JB012132

Boulila S, Vahlenkamp M, De Vleeschouwer D, Laskar J, Yamamoto Y. Towards a robust and consistent middle Eocene astronomical timescale. *Earth Planet. Sci. Lett.* 2018, 486:94–107. DOI: 10.1016/j.epsl.2018.01.003

Brierley CM, Fedorov AV. The relative importance of meridional and zonal SST gradients in explaining Pliocene warmth. *Paleoceanography* 2010, 25(2). DOI: 10.1029/2009PA001809

Burls NJ, Fedorov AV, Jaccard SL, Sigman DM, *et al.* Active Pacific meridional overturning circulation during the warm Pliocene. *Sci. Adv.* 2017, 3(9):e1700156. DOI: 10.1126/sciadv.1700156

Cao Y, Zhang R, Wang S, Kravchinsky VA, Gong H, *et al.* Predominant orbital forcing on Asian hydroclimate during the Miocene Climatic Optimum. *GSA Bull.* 2025, 137(9–10):1–15. DOI: 10.1130/B37776.1

De Schepper S, Gibbard PL, Salzmann U, Ehlers J. A global synthesis of the marine and terrestrial evidence for glaciation during the Pliocene Epoch. *Earth Sci. Rev.* 2014, 135:83–102. DOI: 10.1016/j.earscirev.2014.04.003

Ding Z, Sun J, Liu T, Zhu R, Yang S, *et al.* Wind-blown origin of the Pliocene red clay formation in the central Loess Plateau, China. *Earth Planet. Sci. Lett.* 1998, 161(1–4):135–143. DOI: 10.1016/S0012-821X(98)00145-9

Dowsett H, Dolan A, Moucha R, Rowley D, Alessandro M, *et al.* The PRISM4 (mid-Piacenzian) paleoenvironmental reconstruction. *Clim. Past* 2016, 12(7):1519–1538. DOI: 10.5194/cp-12-1519-2016

Fedorov Av, Burls NJ, Lawrence KT, Pterson LC. Tightly linked zonal and meridional SST gradients over the past five million years. *Nat. Geosci.* 2015, 8(12):975–980. DOI: 10.1038/ngeo2577

Gradstein FM, Ogg JG, Schmitz MD, Ogg GM. *Geologic time scale 2020.* Amsterdam: Elsevier, 2020. pp. 159–192. DOI: 10.1016/B978-0-12-824360-2.00005-X

Hinnov, L. A. Cyclostratigraphy and its revolutionizing applications in the earth and planetary sciences. GSA Bulletin, 2013, 125(11-12):1703-1734. DOI: 10.1130/B30934.1

Huang H, Gao Y, Ma C, Jones MM, Zeeden C, *et al*. Organic carbon burial is paced by a ~173-ka obliquity cycle in the middle to high latitudes. *Sci. Adv.* 2021, 7(28):eabf9489. DOI: 10.1126/sciadv.abf9489

Laskar J. Astrochronology. In *Geologic Time Scale 2020*, 1st Ed. Amsterdam: Elsevier, 2020. pp. 139–158. DOI: 10.1016/B978-0-12-824360-2.00004-8

Laskar J, Fienga A, Gastineau M, Manche H. La2010: long-term astronomical solutions for the motions of the earth. *Astron. Astrophys.* 2011, 532:A89. DOI: 10.1051/0004-6361/201116836

Laskar J, Robutel P, Joutel F, Gastineau M, Correia ACM, *et al.* A long-term numerical solution for the insolation quantities of the Earth. *Astron. Astrophys.* 2004, 428(1):261–285. DOI: 10.1051/0004-6361:20041335

Li M, Hinnov L, Kump L. Acycle: time-series analysis software for paleoclimate research and education. *Comput. Geosci.* 2019, 127:12–22. DOI: 10.1016/j.cageo.2019.02.011.

Li X, Hu Y, Guo J, Lan J, Lin Q, *et al.* A high-resolution climate simulation dataset for the past 540 million years. *Sci. Data* 2022, 9(1):1–10. DOI: https://www.nature.com/articles/s41597-022-01490-4

Li X, Li W, Zhang R, Wei X, Feng Z, *et al.* Intensified East Asian summer monsoon facilitated the formation of the world's largest Late Miocene Hipparion fossil assemblage. *Palaeogeogr. Palaeoclimatol. Palaeoecol.* 2025, 670:112956. DOI: 10.1016/j.palaeo.2025.112956

Li Y, Huang H, Gao Y, Cao Y, Cheng H, *et al.* The ~170 kyr astronomical cycle in the Early Permian Lucaogou Formation of the Junggar Basin. *Front. Earth Sci.* 2024, 12:1272857. DOI: 10.3389/feart.2024.1272857

Lisiecki LE, Raymo ME. A Pliocene-Pleistocene stack of 57 benthic δ18O records. *Paleoceanography* 2005, 20(1). DOI: 10.1029/2004PA001071

Liu Q, Deng C, Yu Y, Torrent J, Zhu R. Quantifying grain-size distribution of pedogenic magnetic particles in Chinese loess and its significance for pedogenesis. *J. Geophys. Res.* 2005, 110(B11). DOI: 10.1029/2005JB003726

Liu Q, Jin C, Hu P, Jiang Z, Ge K, *et al.* Magnetostratigraphy of Chinese loess-paleosol sequences. *Earth Sci. Rev.* 2015, 150:139–167. DOI: 10.1016/j.earscirev.2015.07.009

Ma M, Zhang R, Kravchinsky Va, Wang Y, Bai B, *et al.* Obliquity-modulated monsoon pulses in the northernmost late Eocene red clays of east Asia. *Geophys. Res. Lett.* 2025. (submitted).

Maher B. Palaeoclimatic records of the Chinese Loess Plateau. *Quat. Sci. Rev.* 2016, 154:23–84. DOI: 10.1016/j.quascirev.2016.08.004

Miller CJ, Genovese C, Nichol RC, Wasserman L, Connolly A, *et al.* Controlling the false-discovery rate in astrophysical data analysis. *Astron. J.* 2001, 122(6):3492–3505. DOI: 10.1086/324109

Nie J. The Plio-Pleistocene 405-kyr climate cycles. *Palaeogeography, Palaeoclimatology, Palaeoecology*. 2018, 510:26–30. DOI: 10.1016/j.palaeo.2017.07.022

Nie J, King JW, Fang X. Tibetan uplift intensified the 400 kyr signal in paleoclimate records at 4 Ma. *Geol. Soc. Am. Bull.* 2008, 120(9–10):1338–1344. DOI: 10.1130/B26349.1

Oppo DW, Rosenthal Y, Linsley BK. 2,000-year-long temperature and hydrology reconstructions from the Indo-Pacific warm pool. *Nature* 2009, 460(7259):1113–1116. DOI: 10.1038/nature08233

Qin J, Zhang R, Kravchinsky Y, Valet JP, Sagnotti L, *et al.* 1.2-million-year band of earth-mars obliquity modulation obscured by overlapping Earth-Venus modulation. *J. Geophys. Res.: Solid Earth* 2022, 127(4):e2022jb024131. DOI: 10.1029/2022JB024131

Qu T, Du Y, Strachan J, Meyers G, Slingo J. Sea surface temperature and its variability in the Indonesian region. *Oceanography* 2005, 18(4):50–61. DOI: 10.5670/oceanog.2005.05

Stevens T, Buylaert JP, Thiel C, Újvári G, Yi S, *et al.* Ice-volume-forced erosion of the Chinese Loess Plateau global Quaternary stratotype site. *Nat. Commun.* 2018, 9(1):983. DOI: 10.1038/s41467-018-03329-2

Su Q, Nie J. Intensified Central Asian aridification accompanied with strengthened Asian summer monsoons at the 400-kyr band during 4–2 Ma. *Palaeogeography, Palaeoclimatology, Palaeoecology.* 2024, 649:112342. DOI: 10.1016/j.palaeo.2024.112342

Sun L, Li J, Wang J, Xu Y, Yue L, *et al.* Palaeomagnetic chronology and paleoenvironmental records of late Neogene Wuqi paleolake in northern Chinese Loess Plateau. *Chin. J. Geophys.* 2010, 53(6):1451–1462. DOI: 10.3969/j.issn.0001-5733.2010.06.023

Sun Y, An J, Clemens SC, Bloemendal J, Vandenberghe J, *et al.* Seven million years of wind and precipitation variability on the Chinese Loess Plateau. *Earth Planet. Sci. Lett.* 2010, 297(3,4):525–535. DOI: 10.1016/j.epsl.2010.07.004

Thomson DJ. Spectrum estimation and harmonic analysis. *Proc. IEEE* 1982, 70(9):1055–1096. DOI: 10.1109/PROC.1982.12433

Tian J, Cheng X, Li Q, Wang P, Zhao Q, *et al.* Astronomically modulated Neogene sediment records from the South China Sea. *Paleoceanography* 2008, 23(3). DOI: 10.1029/2007PA001552

Wang H, Shen T, Chen H, Liu X, Nie J. Decoding climate cycles from the Red Clay sequence on the Chinese Loess Plateau. *Quat. Sci. Rev.* 2025, 353:109223. DOI: 10.1016/j.quascirev.2025.109223

Wang H, Lu H, Zhao L, Zhang H, Lei F, *et al.* Asian monsoon rainfall variation during the Pliocene forced by global temperature change. *Nat. Commun.* 2019, 10(1):5272. DOI: 10.1038/s41467-019-13338-4

Weedon GP. Problems with the current practice of spectral analysis in cyclostratigraphy. *Earth Sci. Rev.* 2022, 235:104261. DOI: 10.1016/j.earscirev.2022.104261

Wei X, Zhang R, Kravchinsky VA, Ferraro JV, Qin J, *et al.* Understanding orbital pacing, uplift dynamics, and oceanic influences in aeolian red clay sediments over the Chinese Loess Plateau through cyclostratigraphy insights. *Int. Geol. Rev.* 2025 67(21):2367–2383. DOI: 10.1080/00206814.2025.2528145

Westerhold T, Marwan N, Drury AJ, Liebrand D, Agnini C, *et al.* An astronomically dated record of Earth's climate and its predictability over the last 66 million years. *Science* 2020, 369(6509):1383–1387. DOI: 10.1126/science.aba6853

Wu Q, Zhang R, Li X, Nie J, Liu Z, *et al.* Reorganization of Asian climate in relation to Tibetan Plateau uplift. *Nat. Rev. Earth Environ.* 2022, 3(10):684–700. DOI: 10.1038/s43017-022-00324-5

Wycech J, Kelly DC, Fournelle J, Kitajima K, Kozdon R. Reconstructing Pliocene west Pacific warm pool hydroclimate using in situ microanalyses on fossil planktic foraminifer shells. *Paleoceanogr. Paleoclimatol.* 2020, 35(7):e2019PA003772. DOI: 10.1029/2019PA003772

Xu S, Chen J. Obliquity-paced summer monsoon from the Shilou red clay section on the eastern Chinese Loess Plateau. *Open Geosci.* 2024, 16(1):20220616. DOI: 10.1515/geo-2022-0616

Xu Y, Wang H, Wang J, Sun L, Li J, *et al.* A complete sequence of red clay, lacustrine deposits, and loess on the Eastern Chinese Loess Plateau: implications for the Neogene-Quaternary tectono-geomorphic evolution. *Quat. Int.* 2025, 751. DOI: 10.1016/j.quaint.2025.110035

Zhang L, Kravchinsky VA, Li Y, Sagnotti L, Zhang R, *et al.* Gone with the tilt: obliquity-modulated poleward monsoon pulses in Middle Triassic East Asia. *Geology* 2025. (submitted).

Zhang R, Kravchinsky VA, Qin J, Goguitchaichvili A, Li J. One and a half million yearlong aridity during the Middle Eocenee in NW China. *J. Geophys. Res.: Solid Earth.* 2021, 126(3):e2020JB021037. DOI: 10.1029/2020JB021037

Zhang R, Li X, Xu Y, Sun L, Yue L, *et al.* The 173-kyr obliquity cycle pacing the Asian monsoon in the eastern Chinese loess plateau from late Miocene to Pliocene. *Geophys. Res. Lett.* 2022, 49(2):e2021gl097008. DOI: 10.1029/2021GL097008

Zhang R, Mitchell RN, Wang Y, Orooji Y, Wang Z, *et al.* Northward migration of Earth's rainbelt in East Asia during the middle Eocene. *Nat. Commun.* 2025. (submitted).

Zheng Y, Brierley CM, Burls NJ, Fedorov AV, Zhang R, *et al.* Severe drought in northern east Asia during the early Pliocene. *Geophys. Res. Lett.* 2022, 49(14):e2022GL098813. DOI: 10.1029/2022GL098813